Acta Materialia 242 (2023) 118431

Contents lists available at ScienceDirect

Acta Materialia

journal homepage: www.elsevier.com/locate/actamat

Numerical investigation of dislocation climb under stress and irradiation

D. Da Fonseca[a,d], F. Onimus[b], F. Mompiou[c,d], M.-C. Marinica[a], E. de Sonis[a], E. Clouet[a], T. Jourdan[a,*]

[a] Université Paris-Saclay, CEA, Service de Recherches de Métallurgie Physique, Gif-sur-Yvette, 91191, France
[b] Université Paris-Saclay, CEA, Service de Recherches Métallurgiques Appliquées, Gif-sur-Yvette, 91191, France
[c] Centre d'Elaboration de Matériaux et d'Etudes Structurales, CNRS UPR 8011, 29 rue J. Marvig, BP 94347, Toulouse cedex 4 31055, France
[d] Université de Toulouse, UPS, Toulouse F-31055, France

ARTICLE INFO

Article history:
Received 5 July 2022
Revised 10 October 2022
Accepted 12 October 2022
Available online 15 October 2022

Keywords:
Diffusion
Object kinetic Monte-Carlo
Irradiation creep
Dislocation climb
SIPA

ABSTRACT

We investigate the influence of elastic properties of point defects on dislocation climb under stress and irradiation. For this purpose, elastic dipole tensors and diaelastic polarizabilities are evaluated in aluminum for vacancies and self-interstitial atoms in their stable and saddle configurations, using density functional theory calculations. These parameters are introduced in an object kinetic Monte-Carlo code and a continuous diffusion model to estimate the stress dependence of dislocation climb, using a dipole of straight dislocations. We show that both parameters have an influence on absorption of point defects under stress, in agreement with previous analytical models. However, the effect of dipole tensor is found only 5 times larger than polarizability, whereas models predict a factor up to 30. In addition, including polarizability reverses the stress angular dependence when a uniaxial stress is applied orthogonal to the dislocation line, so in general polarizability cannot be ignored for simulations under applied stress. Further comparison with analytical models shows that they give a good description of angular dependence, provided saddle point configuration of point defects is not too anisotropic. For vacancies, which are strongly anisotropic in their saddle configuration, models fail to reproduce quantitatively lattice effects on stress angular dependence observed in simulations. Calculations show that dislocation climb velocity under irradiation is expected to be the highest if the stress is approximately orthogonal to the dislocation line, especially along the Burgers vector, and the lowest if the stress is applied close to the ⟨100⟩ direction with the largest projection on the dislocation line.

1. Introduction

Under irradiation and applied stress, metallic alloys exhibit a specific deformation process known as irradiation creep [1,2]. The associated strain rate, which may be much larger than the one associated to thermal creep, is related to anisotropic microstructural changes. Among them, anisotropic formation and growth of dislocation loops, resulting from the agglomeration of point defects (self-interstitial atoms, vacancies), have been observed [3–8]. These processes have been explained by the reorientation of small clusters under stress [9] and/or the preferred absorption of self-interstitial atoms (SIAs) and vacancies by some dislocation loops, depending on their orientation with respect to the applied stress [10]. Other mechanisms have also been proposed. They are based on climb-assisted glide of dislocations, whose anisotropic character may also come from the dependence of climb velocity on stress [11].

Two main models have been developed to explain the preferential climb of some dislocation types under applied stress and irradiation. These two models finely depend on the elastic properties of point defects, which couple to the internal and applied strain fields and result in preferential absorption of point defects at some dislocations. They both describe a point defect through its elastic dipole, a tensor which describes how the point defect energy varies in a strain field. The first model, known as stress induced preferred absorption due to anisotropic diffusion (SIPA-AD)[1] [14–17], relies on the anisotropy of dipole tensors of point defects in

* Corresponding author.
E-mail address: thomas.jourdan@cea.fr (T. Jourdan).

[1] In some references it is called SIPA-SAPSE (stress induced preferred absorption due to saddle-point shape effect) [12,13]. This name has the clear advantage to identify the physical quantity responsible for the anisotropic behavior, since anisotropic diffusion (AD) can come from various physical quantities. However,

https://doi.org/10.1016/j.actamat.2022.118431
1359-6454/

their saddle configuration [18]. Due to this anisotropy and to the lowering of crystal symmetry by an applied stress, diffusion becomes anisotropic [19,20]. This anisotropic diffusion is responsible for different absorption "cross-sections" by dislocations and thus for preferred absorption. The second model is the stress induced preferred absorption due to inhomogeneity interaction (SIPA-I). It is also often simply called SIPA, as it was developed first and remains very popular [8,21–23]. It relies on the dependence of dipole tensor on local stress, a phenomenon known as diaelastic polarizability [24].

It is customary to quantify the effect of stress on absorption rate of defects by dislocations by calculating absorption efficiencies, which are key quantities in rate theory models. Previous analytical and numerical calculations have shown that in iron and copper, absorption efficiencies under stress exhibit a higher dependence on elastic dipole anisotropy than on polarizability, so that SIPA-AD could be more than one order of magnitude larger than SIPA-I [12,14,16]. This estimate relies on dipole tensors calculated by interatomic potentials, which can differ substantially from dipole tensors evaluated by *ab initio* methods [25]. Several approximations are made for the polarizability of the elastic dipole to make analytical calculations tractable: the four-rank tensors characterizing this polarizability are assumed to be isotropic and identical for defects at stable and saddle positions. In addition, it is unclear what consequences approximations made in analytical models may have on the absorption rates of point defects [16]. For all these reasons, it appears important to evaluate more precisely the amplitudes of SIPA-AD and SIPA-I, *i.e.* the role of elastic dipole anisotropy and diaelastic polarizabilities on absorption efficiencies of point defects by dislocations under stress.

In the present work, we use two simulation methods to evaluate these absorption efficiencies in aluminum. The first one is an object kinetic Monte-Carlo (OKMC) approach, which has already been used to determine absorption efficiencies without applied stress [26]. The second one is a continuous diffusion model (CDM) [27]. Both methods take into account point defect properties at stable and saddle positions. To obtain a precise value of absorption efficiencies, dipole and polarizability tensors are extracted from density functional theory (DFT) calculations. Aluminum is chosen because it is nearly elastically isotropic, so that isotropic elasticity can be used conveniently to predict absorption efficiencies [26].

This article is organized as follows. In Section 2 diffusion of point defects under stress is discussed and the existing models of absorption efficiency under stress are shortly reviewed. Dipole tensors and diaelastic polarizabilities are calculated in Section 3. Absorption efficiencies of point defects by dislocations are determined by OKMC and CDM and compared to existing models in Section 4.

2. Diffusion of point defects under stress and existing models of point defect absorption efficiency

2.1. Diffusion under stress

The migration of point defects to dislocations depends on their interaction with the elastic field created by dislocations and the applied stress. A point defect can be adequately described as an elastic dipole Π_{ij} [28,29], which depends on the local strain field if it is polarizable (summation over repeated indexes is implied):

$$\Pi_{ij}(\boldsymbol{\varepsilon}) = P_{ij} + \alpha_{ijkl}\varepsilon_{kl}, \tag{1}$$

where $P_{ij} = \Pi_{ij}(0)$ is the elastic dipole without any effect of stress, α_{ijkl} the diaelastic polarizability and ε_{ij} the local strain field at the position of the point defect. The associated interaction energy can be expressed as [30]:

$$E = -P_{ij}\varepsilon_{ij} - \frac{1}{2}\varepsilon_{ij}\alpha_{ijkl}\varepsilon_{kl}. \tag{2}$$

Elastic dipoles and polarizabilities are in general different at stable and saddle positions. In the following, superscript "s" means that a quantity is taken at saddle position.

Dederichs and Schroeder have shown that the point defect flux can be written as a function of a renormalized diffusion tensor [20]

$$\tilde{D}_{ij}(\boldsymbol{r}) = \frac{1}{4}D_0\sum_{\boldsymbol{h}}\hat{h}_i\hat{h}_j\exp\left(-\frac{E^{\mathrm{s},\boldsymbol{h}}(\boldsymbol{r})}{k_\mathrm{B}T}\right), \tag{3}$$

where $E^{\mathrm{s},\boldsymbol{h}}(\boldsymbol{r})$ is the interaction energy as given by Eq. (2) for a point defect initially located at $\boldsymbol{r}$ and performing a jump $\boldsymbol{h}$ with associated unit vector $\hat{\boldsymbol{h}}$, D_0 is the diffusion coefficient without stress, k_B the Boltzmann constant and T the temperature. The strain field in the interaction energy is taken at the location of the saddle point, which in the present case is $\boldsymbol{r}+\boldsymbol{h}/2$. The summation is performed on all nearest neighbors. The stress free diffusion coefficient is $D_0 = \kappa\nu_0 a^2\exp\left(-E_0^\mathrm{m}/k_\mathrm{B}T\right)$, where $\kappa = 1$ for a vacancy and $\kappa = 2/3$ for a $\langle 100\rangle$-split dumbbell SIA. In this expression, a is the lattice parameter of the fcc matrix, ν_0 and E_0^m the attempt frequency and migration energy, respectively.

Using a Taylor expansion to second order in strain of the diffusion coefficient, Woo has clearly shown that different terms contribute to stress induced preferential absorption [16]. Even though in the present work this expansion is not used, it is useful to recall it to make the link with existing models. Let ε_{ij} be the sum of an applied strain $\varepsilon_{ij}^\mathrm{a}$ and an internal strain $\varepsilon_{ij}^\mathrm{d}$ due to a dislocation, which is assumed to weakly vary over distance a, so that $\varepsilon_{ij}^\mathrm{d}(\boldsymbol{r}+\boldsymbol{h}/2) \approx \varepsilon_{ij}^\mathrm{d}(\boldsymbol{r})$. Inserting (2) into (3) leads to

$$\begin{aligned}
\tilde{D}_{ij}(\boldsymbol{r}) \approx\ & \underbrace{D_0\delta_{ij}}_{\text{1 - stress free diffusion}} + \underbrace{\frac{1}{4}D_0\frac{1}{k_\mathrm{B}T}\sum_{\boldsymbol{h}}\hat{h}_i\hat{h}_jP_{kl}^{\mathrm{s},\boldsymbol{h}}\varepsilon_{kl}^\mathrm{d}(\boldsymbol{r})}_{\text{2 - EID, first order}} \\
&+ \underbrace{\frac{1}{4}D_0\frac{1}{k_\mathrm{B}T}\sum_{\boldsymbol{h}}\hat{h}_i\hat{h}_jP_{kl}^{\mathrm{s},\boldsymbol{h}}\varepsilon_{kl}^\mathrm{a}}_{\text{3 - elastodiffusion, SIPA-AD (Woo)}} \\
&+ \frac{1}{4}D_0\frac{1}{k_\mathrm{B}T}\sum_{\boldsymbol{h}}\hat{h}_i\hat{h}_j\Big(\underbrace{\alpha_{klmn}^{\mathrm{s},\boldsymbol{h}}}_{\text{4 - SIPA-I}} + \underbrace{\frac{1}{k_\mathrm{B}T}P_{kl}^{\mathrm{s},\boldsymbol{h}}P_{mn}^{\mathrm{s},\boldsymbol{h}}}_{\text{5 - SIPA-AD (Dederichs)}}\Big)\varepsilon_{kl}^\mathrm{a}\varepsilon_{mn}^\mathrm{d}(\boldsymbol{r}) \\
&+ \underbrace{\frac{1}{4}D_0\frac{1}{k_\mathrm{B}T}\sum_{\boldsymbol{h}}\hat{h}_i\hat{h}_j\left(\frac{1}{2}\alpha_{klmn}^{\mathrm{s},\boldsymbol{h}} + \frac{1}{2}\frac{1}{k_\mathrm{B}T}P_{kl}^{\mathrm{s},\boldsymbol{h}}P_{mn}^{\mathrm{s},\boldsymbol{h}}\right)\varepsilon_{kl}^\mathrm{d}(\boldsymbol{r})\varepsilon_{mn}^\mathrm{d}(\boldsymbol{r})}_{\text{6 - EID, second order}} \\
&+ \underbrace{\frac{1}{4}D_0\frac{1}{k_\mathrm{B}T}\sum_{\boldsymbol{h}}\hat{h}_i\hat{h}_j\left(\frac{1}{2}\alpha_{klmn}^{\mathrm{s},\boldsymbol{h}} + \frac{1}{2}\frac{1}{k_\mathrm{B}T}P_{kl}^{\mathrm{s},\boldsymbol{h}}P_{mn}^{\mathrm{s},\boldsymbol{h}}\right)\varepsilon_{kl}^\mathrm{a}\varepsilon_{mn}^\mathrm{a}}_{\text{7 - elastodiffusion, second order}}.
\end{aligned} \tag{4}$$

The first term corresponds to the diffusion tensor in the absence of stress. The second term, which is related to the elastic interaction difference (EID) for SIAs and vacancies, is responsible for the dislocation bias [31] to first order (second order is the sixth term, it is always neglected). The third term is the classical elastodiffusion term [20]. It has been identified by Woo as the main contribution to SIPA [13,16], called SIPA-AD. The fourth and fifth terms couple the dislocation and applied strains and thus also lead to SIPA. The contribution of polarizability corresponds to SIPA-I effect [21–23], whereas the product of dipole tensors is the SIPA-AD effect

SIPA-AD seems to be more widely used in the literature, so we keep this name here.

as initially considered by Dederichs and Schroeder [20]. In numerical simulations based on dipole tensor anisotropy, both the third and fifth terms are included since the diffusion coefficient is kept in its initial form (3) [15]. Finally, the sixth and seventh terms are second order terms for EID and elastodiffusion. Although the latter can in principle contribute to SIPA, it has been ignored in previous studies based on polarizabilities, which all relied on analytical developments. Only the fourth term was considered. However, here again, the second part of this term is present in numerical studies using anisotropic dipole tensors.

2.2. Models of point defect absorption efficiency under stress

In the framework of rate theory, the effect of stress on point defect absorption rate by dislocations is quantified by the so-called "absorption efficiencies". These quantities relate the absorption rate of point defects to their average concentration in the matrix. They are obtained by solving the diffusion problem around a sink, usually at stationary state [32–36]. Analytical expressions of absorption efficiencies can be obtained only with simple geometries and simplified description of point defect properties. Taking into account the full complexity of Eq. (4) necessarily requires numerical simulations, as those performed in the present work.

Heald and Speight have given an expression for the absorption efficiency of defects by dislocations under a tensile stress of magnitude σ, if among terms 3 to 7 in Eq. (4) only the fourth one is taken into account (SIPA-I) [23]. They assume that the polarizability tensor is the same at stable and saddle points and that it is isotropic, *i.e.*

$$\alpha_{ijkl} = \left(\alpha^K - \frac{2}{3}\alpha^\mu\right)\delta_{ij}\delta_{kl} + \alpha^\mu\left(\delta_{ik}\delta_{jl} + \delta_{il}\delta_{jk}\right), \tag{5}$$

where α^K and α^μ are the bulk and shear polarizabilities [37]. This approximation amounts to considering the defect as an isotropic inhomogeneous Eshelby inclusion in the matrix. The dipole tensor is also assumed to be the same at stable and saddle points and is considered isotropic, *i.e.* $P_{ij} = P\delta_{ij}$. Woo has shown that the expression of Heald and Speight can be cast under the following form (HSW model) [38]:

$$Z^{\mathrm{I}}(\boldsymbol{\sigma}) = Z^0\left(1 + \frac{\Delta Z^{\mathrm{I}}(\boldsymbol{\sigma})}{Z^0}\right), \tag{6}$$

with

$$\frac{\Delta Z^{\mathrm{I}}(\boldsymbol{\sigma})}{Z^0} = \frac{Z^0}{2\pi}\frac{\delta L(\boldsymbol{\sigma})}{L^0} \tag{7}$$

$$Z^0 = \frac{2\pi}{\ln\left(\frac{4R}{|L^0|e^\gamma}\right)} \tag{8}$$

$$L^0 = \frac{Pb}{2\pi}\frac{1-2\nu}{1-\nu}\frac{1}{k_{\mathrm{B}}T} \tag{9}$$

$$\frac{\delta L(\boldsymbol{\sigma})}{L^0} = \frac{\sigma}{\mu}\left[\frac{(1-2\nu)\alpha^K}{2(1+\nu)P} + \frac{\alpha^\mu}{3(1-2\nu)P}\left(-(1+\nu) + 3\nu(\boldsymbol{s}\cdot\boldsymbol{l})^2 + 3(\boldsymbol{s}\cdot\boldsymbol{b})^2\right)\right] \tag{10}$$

(note that the 2π factor in Eq. (7) is missing in the expression of Woo). Z^0 is the absorption efficiency without applied stress. In Eqs. (8)-(10), ν is the Poisson's ratio, μ is the shear modulus, $\boldsymbol{b}$ is the Burgers vector ($b = |\boldsymbol{b}|$), $\boldsymbol{l}$ is the dislocation line direction, γ is the Euler's constant ($\gamma \approx 0.577$) and R is the half-distance between dislocations, calculated as $R = (\pi\rho_{\mathrm{d}})^{-1/2}$ with ρ_{d} the dislocation density. The uniaxial stress is applied along $\boldsymbol{s}$, so that $\sigma_{ij} = \sigma s_i s_j$. Eqs. (6) to (10) are often given with different notations, considering the defect as an Eshelby inhomogenous inclusion. The link between the two formalisms is recalled in Appendix A. For the sake of completeness, we note that an expression with a similar dependence on stress orientation, in $(\boldsymbol{s}\cdot\boldsymbol{l})^2$ and $(\boldsymbol{s}\cdot\boldsymbol{b})^2$, was obtained by Wolfer and Ashkin [37].

With this model, the stress direction leading to the highest absorption efficiency depends on the sign of α^μ/P (Eq. (10)). For an SIA in fcc metals, it is known that in its stable position, $\alpha^\mu > 0$ and $P > 0$ [39], so the model predicts that SIAs are more absorbed by a dislocation if the tensile stress is along the Burgers vector. For a vacancy, it is assumed in the literature that $\alpha^\mu > 0$ [22,23], but $P < 0$, so the reverse behavior is expected.

Later, SIPA due to elastodiffusion (SIPA-AD) was investigated analytically by Skinner and Woo [13], Woo [16], and Borodin and Ryazanov [17]. The most general formula was derived by Borodin and Ryazanov. They showed that if only the three first terms in Eq. (4) are retained, and if the deviatoric part of the dipole tensor at saddle point is small, the absorption efficiency of a defect can be written as

$$Z^{\mathrm{AD}}(\boldsymbol{\sigma}) = Z^0\left(1 + \frac{\Delta Z^{\mathrm{AD},0}}{Z^0} + \frac{\Delta Z^{\mathrm{AD,hydro}}(\boldsymbol{\sigma})}{Z^0} + \frac{\Delta Z^{\mathrm{AD,dev}}(\boldsymbol{\sigma})}{Z^0}\right). \tag{11}$$

Contrary to the SIPA-I model described above, in this model, hereafter called B&R model, the defect has different properties at stable and saddle positions. The absorption efficiency Z^0 is still defined by Eqs. (8) and (9), but P is now related to saddle point properties, *i.e.* $P = P^{\mathrm{s}} = \mathrm{Tr}\,(\boldsymbol{P}^{\mathrm{s}})/3$. Z^0 thus corresponds to the absorption of an isotropic defect at saddle point. Saddle point anisotropy can have an influence on absorption efficiency even in the absence of applied stress [13,15,17,26,40,41], this is taken into account through $\Delta Z^{\mathrm{AD},0}$. The effect of stress on absorption efficiency can be decomposed into an hydrostatic term $\Delta Z^{\mathrm{AD,hydro}}$ depending only on $\mathrm{Tr}\,(\boldsymbol{\sigma})$, and a deviatoric term $\Delta Z^{\mathrm{AD,dev}}$. Only the latter is of interest here, as we focus on the difference of absorption efficiencies for different orientations of applied stress. For a uniaxial stress, it reads [17,42]

$$\frac{\Delta Z^{\mathrm{AD,dev}}(\boldsymbol{\sigma})}{Z^0} = -\frac{\sigma}{4\mu}\frac{P^{\mathrm{s}}}{k_{\mathrm{B}}T} \times\left\{d^{(2)}\left[(\boldsymbol{s}\cdot\boldsymbol{l})^2 - \frac{1}{3}\right] + d^{(3)}\sum_{p=1}^{3}\left[(\boldsymbol{e}_p\cdot\boldsymbol{l})^2(\boldsymbol{e}_p\cdot\boldsymbol{s})^2 - \frac{1}{9}\right]\right\}, \tag{12}$$

where $\boldsymbol{e}_p$ ($p = 1, 2, 3$) are the unit vectors along the crystallographic axes. Factors $d^{(2)}$ and $d^{(3)}$ are related to the components of dipole tensors at saddle point. In an fcc structure, the dipole tensor of a defect jumping along [110] is of the form

$$\boldsymbol{P}^{\mathrm{s}} = \begin{pmatrix} P^{\mathrm{s}}_{11} & P^{\mathrm{s}}_{12} & 0 \\ P^{\mathrm{s}}_{12} & P^{\mathrm{s}}_{11} & 0 \\ 0 & 0 & P^{\mathrm{s}}_{33} \end{pmatrix}. \tag{13}$$

We then have $d^{(2)} = P^{\mathrm{s}}_{12}/P^{\mathrm{s}}$ and $d^{(3)} = (P^{\mathrm{s}}_{11} - P^{\mathrm{s}}_{33})/(2P^{\mathrm{s}}) - P^{\mathrm{s}}_{12}/P^{\mathrm{s}}$.

It appears from Eq. (12) that the absorption efficiency does not depend on the orientation of uniaxial stress with respect to the Burgers vector, unlike SIPA-I. It is generally accepted that what is important for SIPA-AD is the orientation of stress with respect to the dislocation line direction $\boldsymbol{l}$, as shown in the simplified model of Woo [16]:

$$\frac{\Delta Z^{\mathrm{AD,dev}}(\boldsymbol{\sigma})}{Z^0} = \frac{3\sigma}{8\mu}\frac{P^{\mathrm{s}}}{k_{\mathrm{B}}T}\left(1 - \frac{P^{\mathrm{s}}_1}{P^{\mathrm{s}}}\right)\left[(\boldsymbol{s}\cdot\boldsymbol{l})^2 - \frac{1}{3}\right]. \tag{14}$$

This expression corresponds to Eq. (12) if $\boldsymbol{l} = \boldsymbol{e}_p$ for a given p, except that P^{s}_{11} in Eq. (12) is replaced by the eigenvalue P^{s}_1 associated to the eigenvector along the jump direction (in practice P^{s}_{11} and P^{s}_1 are very close, since $P^{\mathrm{s}}_1 = P^{\mathrm{s}}_{11} + P^{\mathrm{s}}_{12}$ and $P^{\mathrm{s}}_{12} \ll P^{\mathrm{s}}_{11}$). For vacancies,

$P^s < 0$ and $P_1^s/P^s > 1$ [26,43], so a tensile stress applied along the dislocation line increases the absorption efficiency. For SIAs, $P^s > 0$ and $P_1^s/P^s > 1$, so the reverse behavior is expected. We note however that in the general case (Eq. (12)), it is clear that the orientation of stress with respect to crystallographic axes also plays a role.

Expressions for SIPA-AD and SIPA-I use only some terms in Eq. (4). In reality, all terms from 3 to 7 contribute to absorption efficiency modification under stress. As shown by Savino and Tomé [14], the third term, as a first-order term, should give the highest contribution. However, their results were obtained with crude estimates of polarizabilities and values of dipole tensors calculated by interatomic potentials. In addition, as shown in the previous paragraphs, various approximations underlie the analytical derivations. That is why, in the following, we evaluate the dipole tensors and polarizabilities for both stable and saddle configurations by DFT and introduce them into an OKMC code and a CDM model, which take into account the full complexity of diffusion under stress. We determine the relative importance of dipole anisotropy and polarizability by comparing these calculations to calculations without polarizability. The validity of expressions (7)-(10) and (12) is discussed, based on our simulation results.

3. Point defect properties

3.1. Method

Point defect properties can be calculated by atomistic simulations, from the energy difference between two simulation boxes containing a point defect, one with applied homogeneous deformation ε and the other one without deformation. Following Eq. (2), it reads, for a box of volume V [29,44],

$$\Delta E(\boldsymbol{\varepsilon}) = \frac{1}{2}\varepsilon_{ij}C_{ijkl}\varepsilon_{kl}V - P_{ij}\varepsilon_{ij} - \frac{1}{2}\varepsilon_{ij}\alpha_{ijkl}\varepsilon_{kl}. \tag{15}$$

The first term corresponds to the homogeneous deformation of the perfect crystal. It can be calculated separately with a dedicated simulation of a box without defect and subtracted from ΔE to retain only the contribution of the point defect. By fitting Eq. (15) without bulk contribution on calculations performed at different deformation levels, for different deformation types (shear, isotropic dilatation, etc.), it is possible to extract point defect dipole and polarizability tensors.

Another method consists in using the average residual stress on the simulation box [29,44]:

$$\sigma_{ij}(\boldsymbol{\varepsilon}) = \frac{1}{V}\frac{\partial \Delta E}{\partial \varepsilon_{ij}} = C_{ijkl}\varepsilon_{kl} - \frac{1}{V}\left(P_{ij} + \alpha_{ijkl}\varepsilon_{kl}\right). \tag{16}$$

Elastic dipoles are readily obtained from simulations with zero applied deformation [45], after subtracting the spurious stress in the perfect simulation box [29]. Polarizabilities can be extracted from a linear fit of the stress as a function of the deformation level, after subtraction of the contribution of the perfect crystal. If the dipole component is also deducted, the quantity $\Delta\sigma_{ij}(\boldsymbol{\varepsilon}) = -\alpha_{ijkl}\varepsilon_{kl}/V$ is obtained.

To evaluate point defect properties in aluminum, DFT calculations are performed with VASP code [46–49] using the projector augmented-wave (PAW) method [50,51]. Calculations are performed including the s states [Ne]$3s^2 3p^1$. The exchange correlation energy is evaluated using the Perdew-Burke-Ernzerhof (PBE) generalized gradient approximation (GGA). The plane wave energy cutoff is set to 400 eV. Brillouin zone integration is performed with a Methfessel-Paxton broadening of 0.4 eV. Supercells with an SIA or a vacancy contain 256 ± 1 atoms. With such simulation cells, a dense shifted Monkhorst-Pack k-point mesh grid of $8 \times 8 \times 8$ points is necessary to obtain converged results, in agreement with previous results [52]. Each configuration is relaxed using the conjugate gradient technique. The climbing image nudged elastic band method (CI-NEB) [53] using 7 images is used in order to find saddle points. A calculation is considered as converged when the forces on each atom are lower than 0.002 eV/Å.

In the present study, dipole tensors are calculated with the stress method (Eq. (16)). Simulations with interatomic potentials with different supercell sizes, reported in supplementary material, show that the error on dipole tensor components due to the interaction between the point defect and its periodic images [25] is less than 1% (Fig. S1 and Table S1). Both energy and stress methods were tested to determine polarizabilities. The convergence with the number of k-points turned out to be faster with the stress method, in agreement with previous observations [54]. In addition, the stress method requires fewer deformation types to extract polarizabilities, since the different stress components are related to different combinations of α_{ijkl} coefficients. For these two reasons the stress method is used. A list of the deformation types, with the corresponding values of $-V\Delta\sigma_{ij}(\boldsymbol{\varepsilon}) = \alpha_{ijkl}\varepsilon_{kl}$, is given in Appendix B. Although the first deformation is not necessary to determine coefficients for cubic and tetragonal symmetries, it is calculated in order to check consistency of coefficients calculated by different deformations. It also gives an estimate of the error on the coefficients, which can roughly be estimated to a few eV. An additional source of error comes from the interaction of the point defect with its periodic images [55]. Simulations with interatomic potentials show that the error on polarizability tensor components with supercells of 256 atoms is less than 10 %, except one component for which it reaches 17 % (Fig. S2 and Table S1). Calculation of polarizabilities at saddle points is computationally demanding, since a NEB calculation must be performed for each deformation level of each deformation type. At least 5 deformation levels are used to perform the fit.

3.2. Results

Dipole and polarizability tensors are given in Table 1. Dipole tensor values are slightly different from a previous DFT study [26], due to different DFT settings and in particular denser k-point meshes used here. They are in good agreement with recent DFT calculations performed on the vacancy [56]. The relaxation volumes, deduced from the dipole tensor values through

$$\Delta V^{\mathrm{r}} = \frac{\mathrm{Tr}\,\boldsymbol{P}}{3K}, \tag{17}$$

where $K = (C_{11} + 2C_{12})/3$ is the bulk modulus, are also presented in Table 1. Altogether the values agree reasonably well with experiments, although the absolute value of the relaxation volume of the vacancy in its stable configuration is larger than the experimental value measured at 4 K. The tetragonal deviation from a cubic dipole tensor for the SIA in its stable configuration is in excellent agreement with the experimental value $P_{11} - P_{22} = 1.1 \pm 0.3$ eV [57].

As can be seen from Eq. (15), introducing polarizable point defects in a material leads to a variation of its elastic constants:

$$\Delta C_{ijkl} = -\frac{x}{\Omega}\alpha_{ijkl}, \tag{18}$$

where x is the atomic fraction of defects and Ω the atomic volume. This can be written under the more convenient form:

$$\frac{\Delta C_{ijkl}}{x C_{ijkl}} = -\frac{1}{\Omega C_{ijkl}}\alpha_{ijkl}. \tag{19}$$

Although α_{ijkl} has a tetragonal symmetry for SIAs, it is not possible to measure all components of the tensor experimentally. Assuming that SIA variants are equally distributed in the material, only data

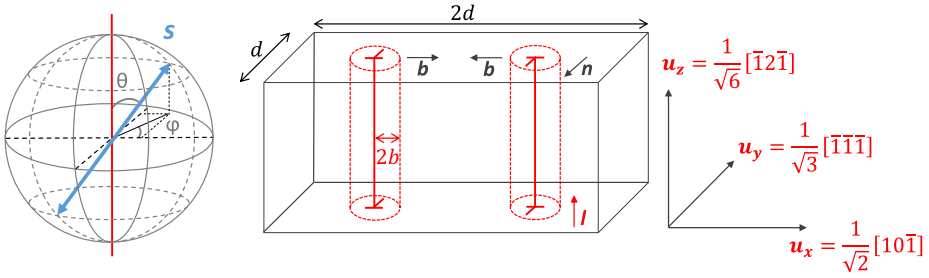

Fig. 1. System simulated containing a dipole of straight dislocations. A tensile stress $\boldsymbol{\sigma}$ is applied along $\boldsymbol{s}$, given by the two angles (θ, φ).

related to cubic symmetry can be extracted. Therefore it is possible to measure two shear polarizabilities

$$\alpha^*_{44} = \frac{1}{3}(\alpha_{44} + 2\alpha_{55}) \tag{20}$$

$$\alpha'^* = \frac{1}{3}\left(\frac{\alpha_{11} - \alpha_{12}}{2} + \frac{\alpha_{22} - \alpha_{12}}{2} + \frac{\alpha_{22} - \alpha_{23}}{2}\right) \tag{21}$$

and a bulk polarizability

$$\alpha^K = \frac{1}{3}\left(\frac{1}{3}(\alpha_{11} + 2\alpha_{12}) + \frac{2}{3}(\alpha_{22} + \alpha_{12} + \alpha_{23})\right). \tag{22}$$

From Eq. (19) it is then possible to compute the influence of defects on C_{44}, $C' = (C_{11} - C_{12})/2$ and K. DFT results in Tab. 1 show that SIAs contribute much more to the change of elastic constants than vacancies, in agreement with experimental results [58]. Vacancies make the material more compliant in compression and in shear, while SIAs are compliant in shear and stiff in compression. These variations are consistent with trends inferred from simple arguments in early works on SIPA-I [23]. The fact that SIAs are compliant in shear, which is not so intuitive, was proved with analytical models and atomistic calculations [59]. Experimental measurements also support this result. The variation in the two shear moduli, C_{44} and C', was measured in aluminum after electron irradiation at low temperature, where only Frenkel pairs are created (Tab. 1). Negative values were obtained, in agreement with present results. We note also that $|\Delta C_{44}/xC_{44}| > |\Delta C'/xC'|$, which has been shown to be typical of fcc metals containing 100-dumbbells [58,59]. Finally and perhaps most importantly, the magnitude of the change of shear moduli due to both vacancies and SIAs agrees well with experimental results. The change in bulk modulus upon introduction of point defects has not been measured in aluminum but it is expected to be small, following results obtained in Cu [60,61]. This is confirmed by our calculations.

We end this section with a comment on the calculation of polarizabilities with interatomic potentials. Early calculations were made with simple pair potentials for stable [59] and saddle [30,62] configurations. The obtained polarizabilities were found consistent with the variation of elastic constants measured experimentally [30,59]. However, later simulations in Cu with more physical potentials were shown to produce results at variance with experiments [55], with values of opposite signs. We encountered similar problems with potentials in aluminum, which highlights the need for DFT calculations to evaluate polarizabilities.

4. Effect of stress orientation on point defect absorption by dislocations

4.1. Methods

In this part, we evaluate the absorption efficiencies of point defects by dislocations in the configuration shown in Fig. 1. The system contains two dislocations of opposite Burgers vectors $\boldsymbol{b} = \pm a/2[10\bar{1}]$ and line direction $\boldsymbol{l} = 1/\sqrt{6}[\bar{1}2\bar{1}]$. The vector normal to the glide plane is $\boldsymbol{n} = 1/\sqrt{3}[111]$. The lattice is rotated to align the dislocations along the direction $\boldsymbol{u}_z$ of the orthorhombic box and the Burgers vectors along $\boldsymbol{u}_x$. The dimension of the system is d along y and $2d$ along x, with $d = 100$ nm, and the dislocations are located at $d/2$ and $3d/2$ along x. This corresponds to a dislocation density $\rho_d = 10^{14}$ m^{-2}, which is typical of steady state dislocation densities of irradiated microstructures [68]. Along z, the system consists of a thin slab of 1 nm. Periodic boundary conditions are used in the three directions. This arrangement of dislocations was used in a previous study [26], it ensures a proper convergence of the strain field when the contribution of dislocations in periodic replica is taken into account [69], if the strain field is evaluated with isotropic elasticity. It has been checked previously that in aluminum, using isotropic elasticity has a negligible effect on absorption efficiencies [26], so we use this approximation here. This also permits to increase the computational efficiency of OKMC simulations. The shear modulus is $\mu = 26$ GPa and the Poisson's ratio is $\nu = 0.35$ [26]. Other dislocation arrangements could have been chosen; with such dislocation densities they would give slightly different values of absorption efficiencies [35]. However, the dependence of absorption efficiencies on stress orientation is expected to be the same.

To determine absorption efficiencies, vacancies and SIAs are considered separately. Point defects are uniformly generated in the system and they are absorbed if they reach one of the cylinders of radius $r_c = 2b$ centered on dislocations. The mean field equation describing the evolution of point defect average concentration $\bar{C}$ is

$$\frac{d\bar{C}}{dt} = G - Z\rho_d D_0 \bar{C}, \tag{23}$$

where G is the creation rate. The absorption efficiency is deduced at steady state from the measurement of $\bar{C}$:

$$Z = \frac{G}{\rho_d D_0 \bar{C}}. \tag{24}$$

A convenient method to determine $\bar{C}$ is object kinetic Monte-Carlo [26]. Point defects are introduced at a constant rate in the simulation box. They perform atomic jumps until they are absorbed by one of the dislocations. For a point defect located at $\boldsymbol{r}$, jump frequencies are calculated for each jump $\boldsymbol{h}$, using the following expression:

$$\Gamma^{\boldsymbol{h}}(\boldsymbol{r}) = \nu_0 \exp\left(-\frac{E_0^m + E^s(\boldsymbol{r} + \boldsymbol{h}/2) - E^e(\boldsymbol{r})}{k_B T}\right), \tag{25}$$

where, as in Section 2, ν_0 and E_0^m are the attempt frequency and the migration energy without elastic interactions, E^e and E^s are the interaction energies with the local strain field at stable and saddle points, respectively (Eq. (2)). Events (defect jumps and creation of point defects) are chosen following the residence time algorithm [70,71]. Transition of SIAs to ⟨110⟩ crowdion configuration, highlighted recently in copper under high local shear strain [72], is

Table 1
Dipole and polarizability tensors of vacancies and SIAs in their stable and saddle configurations. Entries which are not filled are zero by symmetry. Relaxation volumes and change of elastic constants due to defects, deduced from dipole tensors and polarizabilities, respectively, are compared to experimental values. Elastic constants determined by DFT are $C_{11} = 111.4$ GPa, $C_{12} = 60.7$ GPa and $C_{44} = 33.1$ GPa.

	vacancy (stable)	vacancy (saddle) ([100] → [010])	SIA (stable) ([100])	SIA (saddle) ([100] → [010])
P_{11} (eV)	−2.49	−2.15	18.71	18.57
P_{22} (eV)	$= P_{11}$	$= P_{11}$	17.80	$= P_{11}$
P_{33} (eV)	$= P_{11}$	1.96	$= P_{22}$	18.40
P_{12} (eV)		−0.22		1.45
α_{11} (eV)	23	41	−10	4
α_{33} (eV)	$= \alpha_{11}$	-3	−13	−8
α_{44} (eV)	4	7	103	73
α_{55} (eV)	$= \alpha_{44}$	$= \alpha_{44}$	41	$= \alpha_{44}$
α_{66} (eV)	$= \alpha_{44}$	15	$= \alpha_{55}$	62
α_{36} (eV)		9		0
α_{16} (eV)		−1		−12
α_{45} (eV)		10		25
α_{23} (eV)	$= \alpha_{12}$	$= \alpha_{13}$	−45	$= \alpha_{13}$
α_{13} (eV)	$= \alpha_{12}$	2	$= \alpha_{12}$	−56
α_{12} (eV)	13	19	−60	−71
$\Delta V^r/\Omega$ (sim.)	−0.31	−0.10	2.27	
$\Delta V^r/\Omega$ (exp.)	-0.05 ± 0.05[a]	−0.19[d]	1.9 ± 0.2[a,c]	
	−0.36[b]			
$\frac{\Delta C_{44}}{xC_{44}}$ (sim.)	−1.2		−18.1	
$\frac{\Delta C_{44}}{xC_{44}}$ (exp.)[e]			-23 ± 2	
$\frac{\Delta C'}{xC'}$ (sim.)	−1.9		−8.2	
$\frac{\Delta C'}{xC'}$ (exp.)[e]			-13 ± 2	
$\frac{\Delta K}{xK}$ (sim.)	−2		5	

[a] Measurement at 4 K, Reference [63].
[b] Measurement at 700 K, Reference [64].
[c] Reference [65].
[d] Reference [66], using formation volume of Ref. [64].
[e] After subtraction of the anharmonic effect due to volume expansion [58]. This value corresponds to the sum of SIA and vacancy contributions, but it is often considered that vacancy contribution is small [39,58], which is confirmed by measurements on quenched samples [67].

not considered. More details on OKMC simulations can be found in Ref. [26].

For a given creation rate, it is possible to determine Z by calculating the average number of point defects in the simulation box at steady state (Eq. (24)). The physical time of the simulations is chosen to ensure the convergence of Z. To provide a confidence interval, the standard deviation is computed with a block-averaging procedure [73]. On all graphs, the error bars in figures correspond to the standard deviation.

An alternative to OKMC is the continuous diffusion model (CDM), as described in Ref. [27]. This approach has been shown to produce results in close agreement with reference OKMC simulations; in particular, it can properly handle the interaction of point defects with sinks in their stable and saddle positions, as explicitly done in OKMC. The equation to be solved is based on the expression of the renormalized diffusion tensor given in Eq. (3):

$$G - \nabla \cdot \boldsymbol{J} = 0, \tag{26}$$

with

$$\boldsymbol{J}(\boldsymbol{r}) = -\tilde{\boldsymbol{D}}(\boldsymbol{r}) \nabla u(\boldsymbol{r}). \tag{27}$$

In this equation, u is a renormalized concentration, which accounts for the concentrations of the different configurations of defects in their stable position (for SIAs) [20,27]. Contrary to OKMC, CDM is a local approach, *i.e.* it amounts to taking E^s in Eq. (25) at $\boldsymbol{r}$ instead of $\boldsymbol{r} + \boldsymbol{h}/2$. In practice, for weakly varying elastic fields, this approximation is valid. CDM calculations are similar to phase field calculations in this context [41].

Since it is deterministic in nature, CDM produces results which are free of statistical error. However, the finite element solving of the continuity equation (26) may be quite CPU and memory demanding for large three-dimensional systems, as fine meshing is required near the sink where concentrations and elastic fields vary steeply. Therefore, this method is especially useful for systems which are invariant along at least one direction. This is the case of the configuration shown in Fig. 1, which is invariant along z. Although absorption efficiencies can be obtained with a two-dimensional system, we use a thin slab of 1 nm along z and impose periodic boundary conditions, as in OKMC.

In the following, simulations are performed at $T = 300$ K. A uniaxial tensile stress of 100 MPa is applied along (θ, φ) (Fig. 1). Although this value is rather high for aluminum (the yield stress of very large grained pure aluminum is around 10 MPa), it permits to obtain a better convergence with OKMC. We have checked, by varying the stress amplitude, that at such levels of stress the absorption efficiency is linear in σ. So the results can easily be extrapolated to lower values of stress. The effect of elastodiffusion is investigated with OKMC, which is our reference method. We check that in this case, CDM produces results in agreement with OKMC. To determine the effect of polarizability, we subtract the absorption efficiencies obtained with and without polarizability. As we need very high accuracy on the absorption efficiencies to perform the subtraction, CDM is used in this case.

4.2. Results

4.2.1. SIPA-AD

As explained above, for SIPA-AD the interaction energy of point defects is based solely on elastic dipoles. To evaluate this first mechanism, we start with OKMC simulations. A 3D map represent-

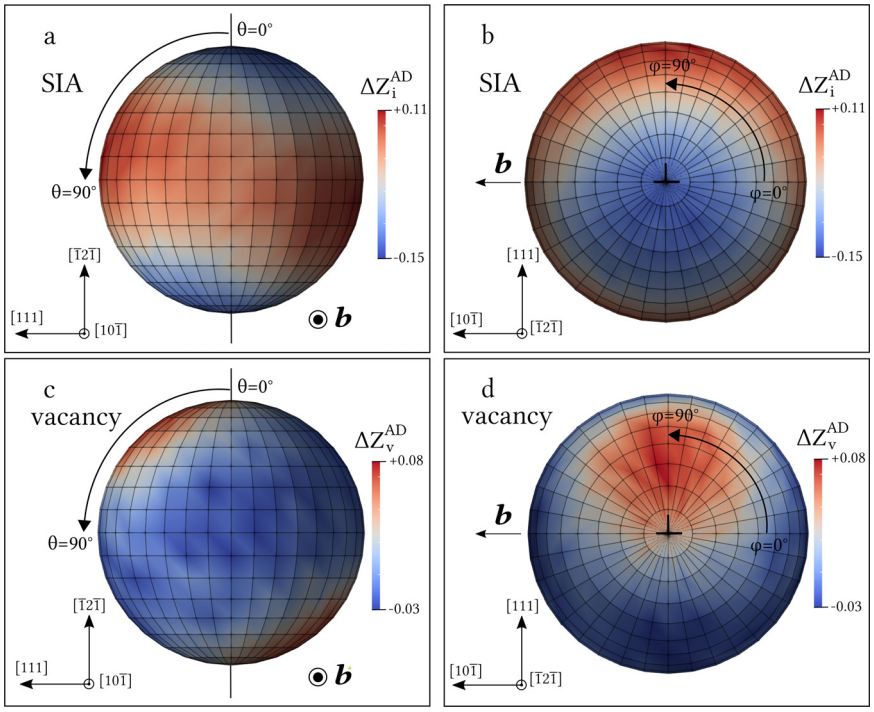

Fig. 2. Difference of absorption efficiency ΔZ^{AD} (see text for the definition) of a straight dislocation dipole in relation to the tensile stress orientation, represented on a unit sphere by a color scale for SIPA-AD mechanism when only P_{ij} is accounted for in the interaction energy. A tensile stress of 100 MPa is applied, scanning space with a 10° step. The dislocation is along $[\bar{1}2\bar{1}]$ and the Burgers vector is along $\pm[10\bar{1}]$. The SIA results are presented in (a) and (b) and the vacancy results in (c) and (d). For the sake of clarity only one dislocation is schematically represented.

ing the influence of tensile stress orientation on absorption efficiency is shown in Fig. 2. We represent the difference of absorption efficiencies for a uniaxial stress of magnitude σ and a hydrostatic stress with the same value of $\mathrm{Tr}(\boldsymbol{\sigma})$, called ΔZ_i^{AD} for SIAs and ΔZ_v^{AD} for vacancies. This quantity corresponds to $\Delta Z^{AD,dev}$ in the decomposition shown in Eq. (11). From Fig. 2 we see that vacancy absorption is increased if the stress is applied close to a direction ($\theta = 30°, \varphi = 90°$). Directions that favor SIA absorption are more or less spread on a strip tilted with respect to the plane orthogonal to the line direction.

To provide a more quantitative representation and facilitate the comparison with CDM and B&R model (Eq. (12)), ΔZ^{AD} is plotted in Figs. 3 and 4 as a function of θ, for $\varphi = 0°$ (in the slip plane $(\boldsymbol{l}, \boldsymbol{b})$) and $\varphi = 90°$ (in the climb plane $(\boldsymbol{l}, \boldsymbol{n})$). Results obtained with CDM are in very good agreement with OKMC, which validates CDM to calculate sink strengths in this configuration. B&R model is able to qualitatively reproduce the effect of stress on absorption efficiency. In particular, the dependence on φ is correctly taken into account, unlike the model of Woo which only depends on θ (not shown). However, the amplitude of ΔZ^{AD} is underestimated with B&R model, especially for the vacancy with a factor up to 3 at $\theta = 30°$ and $\varphi = 90°$, where the absorption efficiency is maximum.

4.2.2. SIPA-I

To determine the effect of polarizability, absorption efficiencies obtained with dipole tensors only are subtracted from those obtained with both dipole and polarizability tensors taken into account. These quantities are noted ΔZ^{I}. As discussed above, CDM is used for the two calculations to obtain results free from statistical errors.

Absorption efficiencies of SIAs and vacancies are the highest along two different specific directions of applied stress (Fig. 5). Absorption of SIAs is more efficient if the stress is applied along the Burgers vector, in agreement with early estimates of SIPA-I [21,23,38]. The influence of polarizability on vacancy absorption under stress is more surprising. It appears quite similar to the effect of dipole tensor anisotropy, with a direction of preferential absorption along ($\theta = 30°$, $\varphi = 90°$). With the existing SIPA-I model, one expects a low absorption rate if the stress is applied along the Burgers vector and a higher absorption rate for other stress orientations.

To provide a more quantitative comparison with HSW model (Eqs. (7)-(10)), which assumes that point defects have the same isotropic properties at stable and saddle positions, the values of dipole tensor P and polarizabilities α^{μ} and α^{K} are deduced from properties of defects in Tab. 1 taken at stable position. P, calculated as $\mathrm{Tr}(\boldsymbol{P})/3$, is equal to 18.10 eV for SIAs and −2.49 eV for vacancies. Shear polarizability can be expressed as a Voigt average

$$\alpha^{\mu} = \frac{3}{5}\alpha_{44}^{*} + \frac{2}{5}\alpha'^{*}, \tag{28}$$

where α_{44}^{*} and α'^{*} are given by Eqs. (20) and (21) respectively. We have $\alpha^{\mu} = 45.6$ eV for SIAs and $\alpha^{\mu} = 4.4$ eV for vacancies. Bulk polarizability, as calculated with Eq. (22), is $\alpha^{K} = -40.7$ eV for SIAs and $\alpha^{K} = 16.3$ eV for vacancies.

The effect of SIPA-I is usually discussed for a tensile stress orthogonal to the dislocation line ($\theta = 90°$), either along the Burgers vector ($\varphi = 0°$) or orthogonal to it ($\varphi = 90°$) [23]. The variation of absorption efficiency with φ, with $\theta = 90°$, is shown in Figs. 6 and 7 for SIAs and vacancies, respectively. Some terms are dropped in Eq. (6), which may explain why results are shifted with respect to CDM. This shift is not relevant to our purpose. Leaving this aspect aside, the agreement between CDM results and HSW model for $\theta = 90°$ is remarkable for the two defects. Results for $\theta = 30°$, including the direction where ΔZ_v^{I} is maximum, are also reported in these figures. The analytical solution departs appreciably from CDM, especially for the vacancy. The amplitude of SIPA-I for the vacancy is lower than the result from CDM by more than a factor two.

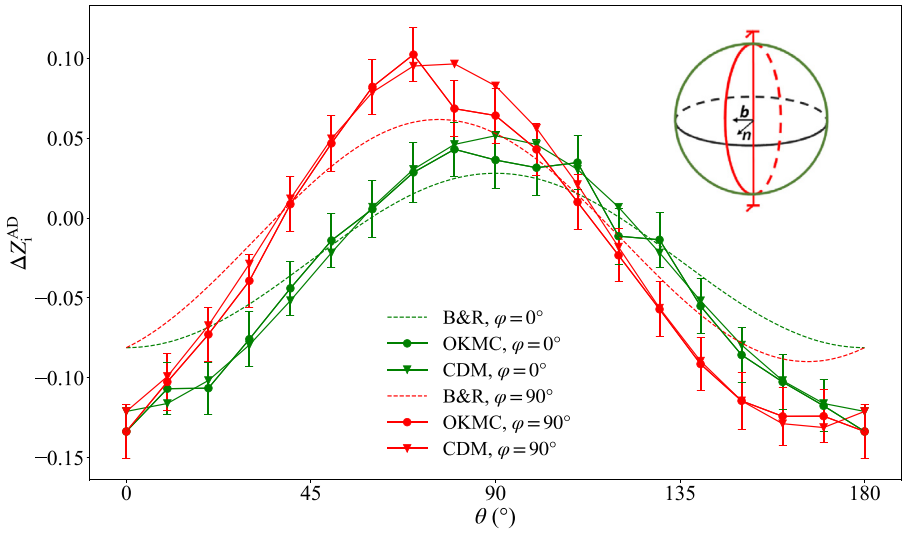

Fig. 3. Difference of absorption efficiency ΔZ^{AD} (see text for the definition) of a straight dislocation dipole for SIAs as a function of θ (angle between tensile stress and dislocation line $\boldsymbol{l}$) for SIPA-AD mechanism, with only P_{ij} accounted for in the interaction energy. Results obtained by OKMC and CDM are compared. The analytical B&R model of Eq. (12) is shown in dashed lines. The absorption efficiency is presented for two values of φ: $\varphi = 0°$, *i.e.* in a plane containing $\boldsymbol{l}$ and $\boldsymbol{b}$ and $\varphi = 90°$, *i.e.* in a plane containing $\boldsymbol{l}$ and $\boldsymbol{n}$.

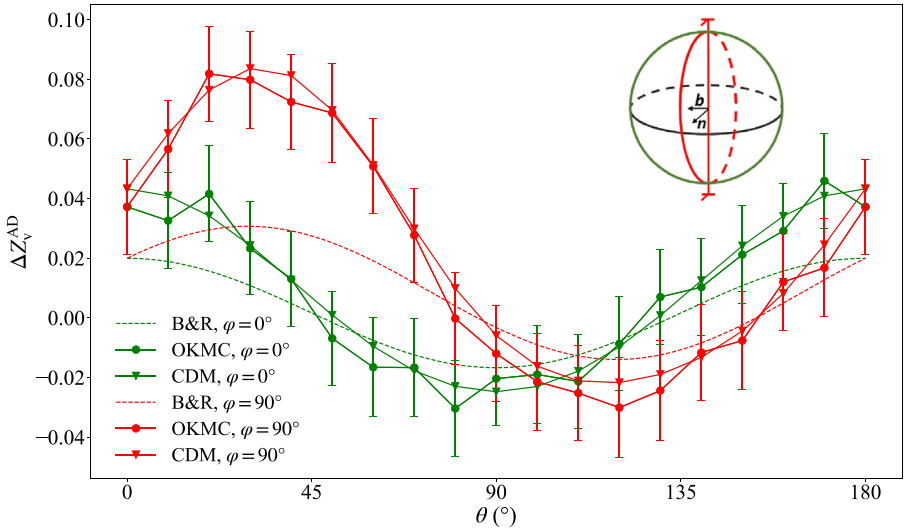

Fig. 4. Difference of absorption efficiency ΔZ^{AD} (see text for the definition) of a straight dislocation dipole for vacancies as a function of θ (angle between tensile stress and dislocation line $\boldsymbol{l}$) for SIPA-AD mechanism, with only P_{ij} accounted for in the interaction energy. Results obtained by OKMC and CDM are compared. The analytical B&R model of Eq. (12) is shown in dashed lines. The absorption efficiency is presented for two values of φ: $\varphi = 0°$, *i.e.* in a plane containing $\boldsymbol{l}$ and $\boldsymbol{b}$ and $\varphi = 90°$, *i.e.* in a plane containing $\boldsymbol{l}$ and $\boldsymbol{n}$.

4.3. Discussion

4.3.1. SIPA-AD

The contribution of intrinsic dipole anisotropy at saddle configuration to SIPA (SIPA-AD) has been discussed by several authors [13,15–17,19,20]. It was shown that the absorption efficiency is mostly dependent on the direction of uniaxial stress with respect to the dislocation line [13,15]. Under stress, the diffusion tensor becomes anisotropic, owing to saddle point anisotropy. A dislocation orthogonal to the direction of fastest diffusion will capture more point defects than a dislocation collinear to it, because its "cross section" for defect absorption is higher (the term "cross-section" is only strictly valid for purely 1D diffusion, *i.e.* for an infinitely large effect of stress). Directions of fast diffusion depend on the values of dipole tensor at saddle configuration. Vacancies diffuse preferentially in a plane orthogonal to the applied stress [74], which explains why vacancy absorption is enhanced when the tensile direction is collinear to the dislocation line. The behavior of SIAs is explained with the same reasoning [16].

We have seen in Fig. 2 that our simulations and B&R model are in qualitative agreement with these conclusions. However, the direction of maximum absorption of vacancies is shifted by about 30° with respect to the line direction in the plane defined by $(\boldsymbol{l}, \boldsymbol{n})$ $(\varphi = 90°)$. Likewise, the strip of maximum absorption for SIAs is tilted, with a maximum at around $\theta = 70°$ in the plane $(\boldsymbol{l}, \boldsymbol{n})$ and $\theta = 90°$ in the plane $(\boldsymbol{l}, \boldsymbol{b})$ $(\varphi = 0°)$. These discrepancies can be explained by lattice effects, which are not all taken into account in Woo's approach (Eq. (14)), unlike B&R model (Eq. (12)).

To explain these results, we consider a uniaxial stress $\sigma_{ij} = \sigma s_i s_j$, with $s_1 = \sin\alpha\cos\beta$, $s_2 = \sin\alpha\sin\beta$, $s_3 = \cos\beta$ the three direction cosines of $\boldsymbol{s}$ in the basis ([100],[010],[001]). We have

$$\varepsilon_{ij} = \frac{\sigma}{E}\left(s_i s_j(1+\nu) - \nu\delta_{ij}\right), \tag{29}$$

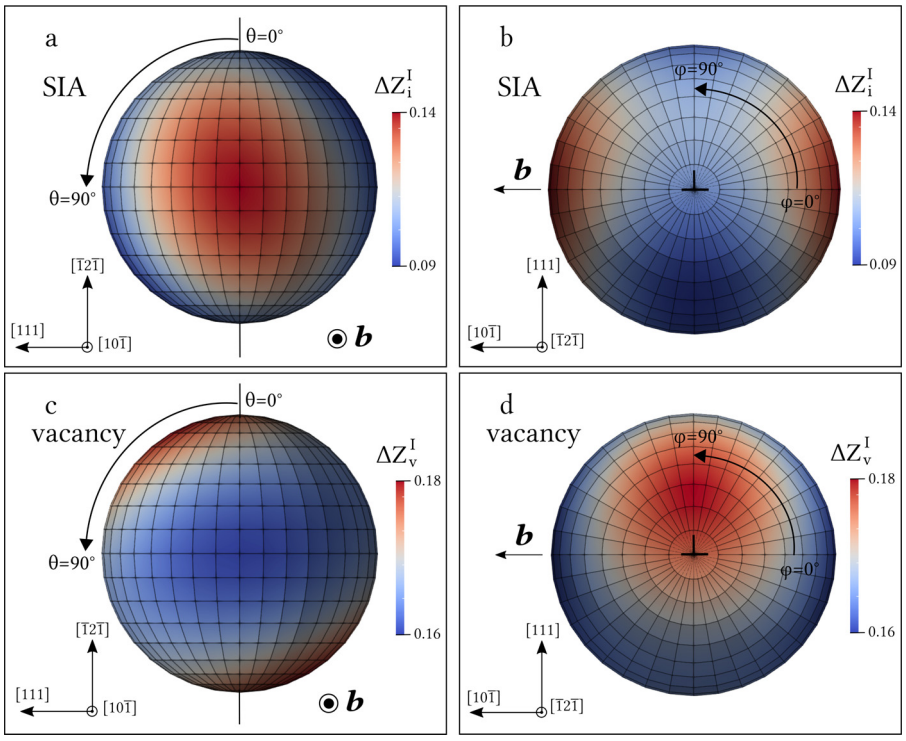

Fig. 5. Absorption efficiency increment ΔZ^I of point defects by a straight dislocation dipole in relation to the tensile stress orientation, represented on a unit sphere by a color scale, due to polarizability α_{ijkl} (SIPA-I). Values are obtained by CDM. They result from the difference between absorption efficiencies with P_{ij} and α_{ijkl} considered and with only P_{ij} included. A tensile stress of 100 MPa is applied, scanning space with a 10° step. The dislocation is along [$\bar{1}2\bar{1}$] and the Burgers vector is along ±[10$\bar{1}$]. The SIA results are presented in (a) and (b) and the vacancy results in (c) and (d).

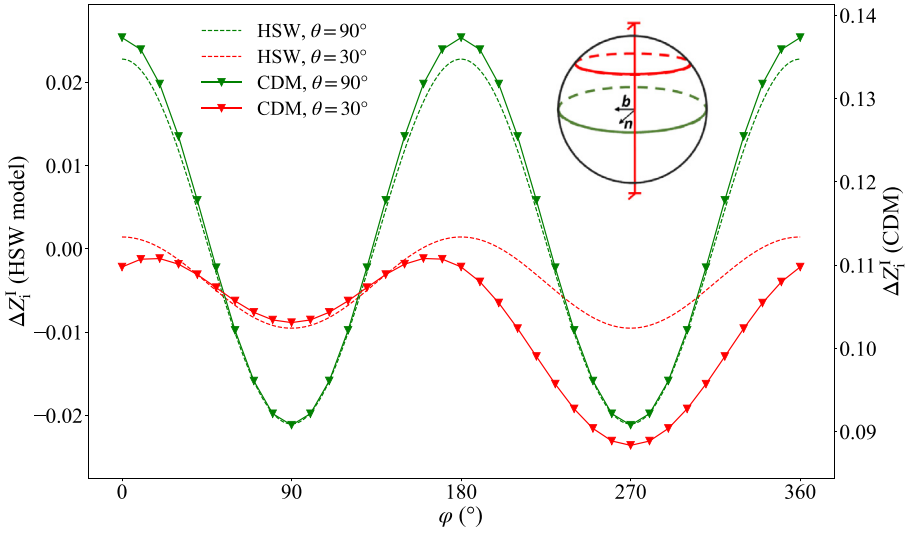

Fig. 6. Increment of absorption efficiency ΔZ_i^I due to polarizability of SIAs, as a function of φ, for two values of θ (30° and 90°). Results are obtained with CDM and compared to HSW model given by Eqs. (7)-(10).

with $E = 2\mu(1+\nu)$ Young's modulus. We consider a jump along [110], for which the dipole tensor at saddle position is given by Eq. (13). Neglecting the polarizability, the saddle point energy reads

$$E^s = -\frac{\sigma}{E}\Big(P_{11}(1+\nu)\sin^2\alpha - 2\nu P_{11} + P_{33}(1+\nu)\cos^2\alpha - \nu P_{33} + P_{12}(1+\nu)\sin^2\alpha\sin 2\beta\Big). \quad (30)$$

Given the signs of the dipole tensor components of a vacancy (see Tab. 1), it is clear that the energy is minimum for $\alpha = 0°$, *i.e.* for a stress applied along [001]. For the SIA, since $P_{12} > 0$, we must have $\beta = 45°$. In addition, with $P_{11} + P_{12} > P_{33}$ the energy is minimum for $\alpha = 90°$. This means the stress must be applied along the jump direction to minimize the saddle point energy.

As already discussed, to obtain the maximum absorption efficiency by a dislocation, one must favor the jumps which are as orthogonal as possible to this dislocation. For a dislocation along $\boldsymbol{l} = [\bar{1}2\bar{1}]/\sqrt{6}$, there are two jumps which are orthogonal to the dislocation line, highlighted in red in Fig. 8-(a). These jumps are favored if the stress is applied along [010]. This configuration corresponds to $\theta = 35°$, in close agreement with our OKMC and CDM results ($\theta \approx 33°$) and B&R results ($\theta = 29°$). The absorption rate of

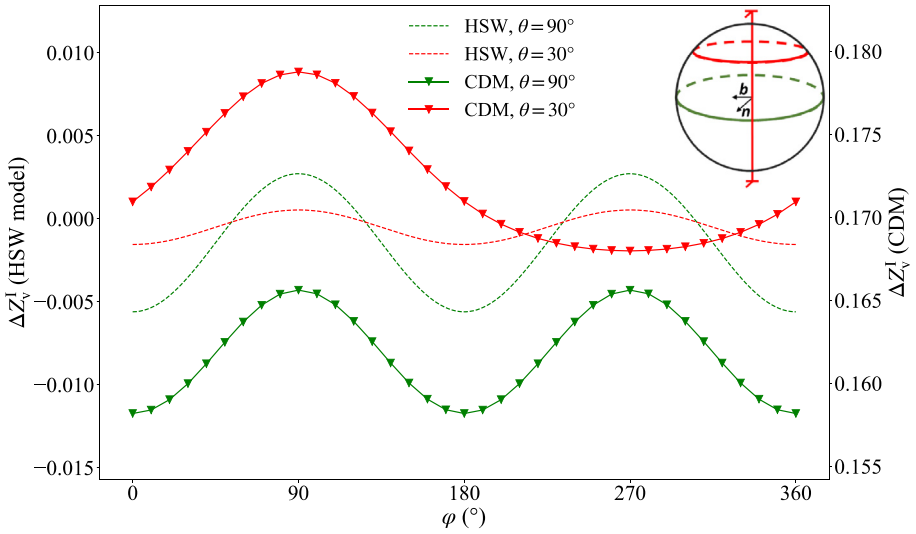

Fig. 7. Increment of absorption efficiency ΔZ_v^I due to polarizability of vacancies, as a function of φ, for two values of θ (30° and 90°). Results are obtained with CDM and compared to HSW model given by Eqs. (7)-(10).

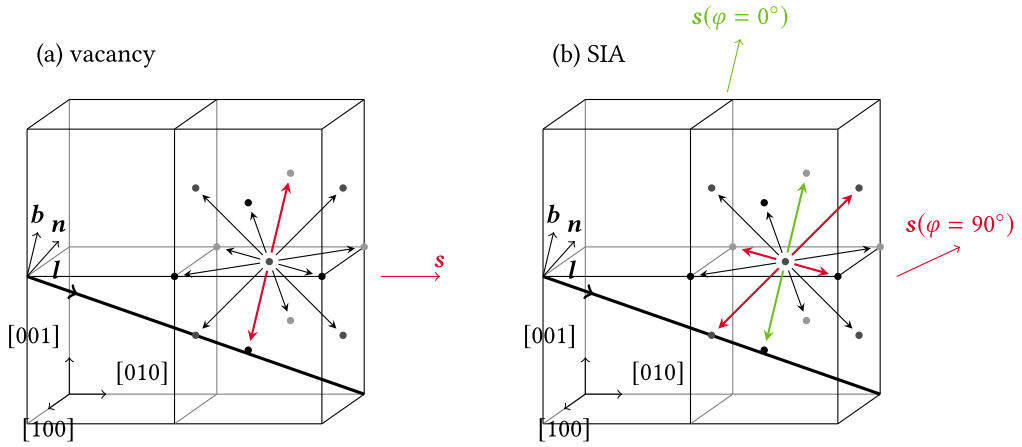

Fig. 8. Orientation of uniaxial stress $\boldsymbol{s}$ leading to maximum absorption of point defects by a dislocation of line direction $\boldsymbol{l} = [\bar{1}2\bar{1}]/\sqrt{6}$ and Burgers vector $\boldsymbol{b} = [\bar{1}01]/\sqrt{2}$ ($\boldsymbol{n} = [111]/\sqrt{3}$), and associated jumps responsible for this high absorption rate. (a) Absorption of vacancies (b) Absorption of SIAs; here we give the orientation of stress if it is applied in the planes defined by $(\boldsymbol{l}, \boldsymbol{b})$ ($\varphi = 0°$) and $(\boldsymbol{l}, \boldsymbol{n})$ ($\varphi = 90°$). The maximum absorption rate is obtained in this latest case, with four jumps contributing significantly to the absorption of SIAs.

SIAs should be large if the stress is applied along the direction of the two jumps orthogonal to the line direction, represented in green in Fig. 8-(b). The jump direction is along $\boldsymbol{b}$, and it can be seen in Fig. 2 that indeed, this direction is located in the strip of high absorption rates. It is actually the direction of highest absorption rate in the plane $(\boldsymbol{l}, \boldsymbol{b})$ ($\varphi = 0°$). From Fig. 2 it appears that maximum absorption rates are obtained in a plane $(\boldsymbol{l}, \boldsymbol{n})$ ($\varphi = 90°$). For a stress applied in this plane, the projection of $\boldsymbol{s}$ on the jumps represented in red in Fig. 8-(b) is the highest for $\theta = 71°$; these four jumps are not orthogonal to the dislocation, but their projection on $\boldsymbol{l}$ is small. The fact that four jumps contribute to SIA diffusion enhancement in this case explains why the absorption rate is even higher than for $\boldsymbol{s}$ along $\boldsymbol{b}$. The value of θ found is very close to OKMC and CDM results ($\theta = 76°$, Fig. 3) and B&R results ($\theta = 76°$). The variation of θ from 90° to 71° as φ varies from 0° to 90° explains the tilted strip in Fig. 2. Finally, we note that in this discussion, the strain field of the dislocation has not been considered. This validates the assumption of Woo to neglect the dislocation field in the analytical treatment [16]. Fully considering lattice effects as in B&R model appears necessary to obtain a good agreement with OKMC and CDM. We note that although second order terms in Eq. (4) (fifth term and second part of seventh term) can in principle also contribute to SIPA-AD, they certainly have a very small impact as they are included in OKMC and CDM but not in B&R model.

Even though B&R model successfully reproduces lattice effects, the magnitude of ΔZ^{AD} is significantly different from our calculations for both defects. This is especially the case for the vacancy. In the direction of applied stress where the absorption efficiency is the highest, the discrepancy reaches a factor of around 3. For this direction, the effects of anisotropy of dipole tensor at saddle configuration are the highest. In the model developed by Borodin and Ryazanov, the deviatoric part of the dipole tensor is assumed to be small compared to the hydrostatic part. This is not true for the vacancy, so it is not surprising that the model cannot quantitatively reproduce the values of ΔZ^{AD} when the dipole anisotropy contributes significantly to the absorption efficiency.

4.3.2. SIPA-I

Contrary to SIPA-AD, the dislocation strain field is an essential ingredient in SIPA-I. The fourth term in Eq. (4), which in-

duces a coupling between the applied field and the dislocation field, gives rise to preferential diffusion of point defects to some dislocations. Usually, one considers that SIAs are the main contributors to SIPA-I, due to their large polarizability [14,38,75–77]. HSW model (Eqs. (7)-(10)) predicts that SIAs will be absorbed preferentially by dislocations whose Burgers vector is aligned with the applied stress [22,23,38].

Our DFT calculations confirm that SIAs are much more polarizable than vacancies (Tab. 1). Shear polarizabilities of SIAs and vacancies at stable point, which are used in the analytical model, are found to differ by around one order of magnitude. However, the effect of vacancies on SIPA-I is not completely negligible (Fig. 5): the amplitude of the effect is only three times smaller than for SIAs. This is essentially due to the high absorption efficiency of vacancies when the stress is applied in the plane $(\boldsymbol{l}, \boldsymbol{n})$, for $\theta = 25°$, close to the direction corresponding to a maximum of absorption efficiency for SIPA-AD ($\theta = 33°$). This behavior is not captured by HSW model. Additional calculations (not shown) performed with CDM and using isotropic and identical properties at stable and saddle points led to results in close agreement with HSW model. We can conclude that this model is accurate in its framework and that the discrepancy observed here is certainly due to lattice effects. On the contrary, the agreement between the model and CDM is rather satisfactory for SIAs, although some discrepancies appear if the stress is not normal to the dislocation line. This shows that in general, since polarizabilities induce second order contributions, they should not be considered without taking into account the first order contributions, *i.e.* of dipole anisotropy. To our knowledge, our simulations are the first estimations of SIPA-I based on full account of first order terms and polarizabilities at saddle configurations.

As for SIPA-AD, other terms potentially contributing to SIPA are included in CDM but not in the model. The first part of the seventh term in Eq. (4) leads to anisotropic diffusion, so to SIPA. However, for applied strains of the order of 10^{-4} as those considered here, this term can be safely neglected.

4.3.3. Relative contributions of SIPA-AD and SIPA-I to dislocation climb under stress

From analytical expressions as (6) and (11), it has been suggested that SIPA-AD is up to thirty times larger than SIPA-I [12,14,16]. It is interesting to see whether the present calculations, with more accurate values of dipole tensors and polarizabilities, confirm this conclusion. Indeed, considering polarizabilities induces additional complexity in kinetic codes, so it is useful to assess the relevance of including them. From Figs. 2 and 5, one sees that the amplitude of absorption efficiencies considering intrinsic dipole anisotropy only (SIPA-AD) is around five times larger than the one due to polarizability (SIPA-I), whatever the defect. However, as shown in Fig. 9, for a stress applied in a plane normal to the dislocation line, polarizability reverses the directions of favored absorption of SIAs. The reason for this is the low effect of dipole anisotropy in this plane, at variance with polarizability. This suggests that polarizabilities cannot be disregarded for studies under stress.

Including intrinsic dipole anisotropy and polarizability in the calculations permits to conclude about the directions of applied stress which favor SIA or vacancy absorption. From the present results it can be concluded that if the stress is approximately orthogonal to the dislocation line, and in particular along the Burgers vector, the net absorption rate of SIAs should be the highest. On the contrary, a uniaxial stress applied close the ⟨100⟩ direction with the largest projection on the dislocation line should minimize the net absorption rate of SIAs. Since climb velocity under irradiation is generally driven by an excess of absorbed SIAs due to EID, the climb velocity is expected to increase in the first configuration and to decrease in the second one.

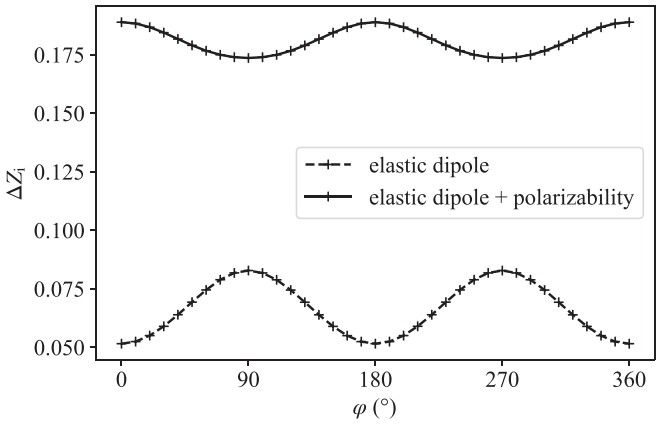

Fig. 9. Difference of absorption efficiency of SIAs ΔZ_i as a function of φ, calculated with CDM for $\theta = 90°$. The reference calculation which is subtracted corresponds to a hydrostatic stress with only P_{ij} taken into account. The dashed curve shows the evolution of ΔZ_i if only P_{ij} is taken into account and the solid curve corresponds to the case where P_{ij} and α_{ijkl} are considered.

5. Conclusion

In this study we have investigated the effect of an applied uniaxial stress on point defect absorption by straight dislocations in aluminum. Elastic dipoles and diaelastic polarizabilities of vacancies and SIAs have been calculated by DFT at stable and saddle points. These parameters have been used in an OKMC code and a CDM model to evaluate absorption efficiencies under stress. Our results confirm that the amplitude of SIPA-I, due to polarizability, is lower than the one of SIPA-AD, due to dipole anisotropy, by a factor of around five. However, the correct behavior of the absorption efficiency in a plane orthogonal to the dislocation line can only be obtained if polarizability is considered, so neglecting polarizability in studies under stress may not be appropriate.

Simulation results have been compared to analytical expressions of SIPA-AD and SIPA-I. For SIAs, models are shown to be in reasonable agreement with simulations. Vacancies are very anisotropic in their saddle configuration, which induces strong lattice effects on the diffusion under stress. In this case the predictions of the models are not very accurate. The expression of Borodin and Ryazanov (B&R) for SIPA-AD includes lattice effects but it is assumed that defects are weakly anisotropic in their saddle configuration. It correctly predicts a maximum absorption rate of vacancies if the stress is applied along the ⟨100⟩ direction with the largest projection on the dislocation line. However, the amplitude of SIPA-AD is underestimated by a factor 3. The expression for SIPA-I given by Woo (HSW model) relies on a simple isotropic description of defects and is unable to reproduce the angular dependence of absorption efficiency, which is similar to that of SIPA-AD.

Our results show that dislocation climb velocity under irradiation is expected to be the highest if the stress is approximately orthogonal to the dislocation line, especially along the Burgers vector, and the lowest if the stress is applied close to the ⟨100⟩ direction with the largest projection on the dislocation line. The dependence of these results on the symmetries of point defects in their saddle configuration makes these conclusions likely transferable to other fcc metals. The methodology used in this work can be applied to Frank dislocation loops. It would be interesting to compare the obtained results to experimental measurements of loop

growth rates under stress [7], to better assess irradiation creep mechanisms.

Data availability

The relevant data are available within the article or from the authors upon reasonable request.

Declaration of Competing Interest

The authors declare that they have no known competing financial interests or personal relationships that could have appeared to influence the work reported in this paper.

Acknowledgments

T. J. acknowledges F. Willaime for discussions about DFT calculations and Y. Le Bouar for discussions about polarizabilities. This work was performed using HPC resources from GENCI-CINES (Grant 2020-A0100912414).

Appendix A. Modelling point defects as inhomogeneous inclusions

SIPA-I expressions (6)-(10) are more often given with notations related to Eshelby inhomogenous inclusions. In this framework, a defect is considered as a spherical inhomogeneity of bulk and shear moduli K^* and μ^*, respectively, with a misfit corresponding to the transformation strain e^*_{ij}. It is convenient to consider an equivalent homogeneous inclusion of transformation strain e^{T}_{ij}, which depends on e^*_{ij} and on the local external strain field (sum of the dislocation and applied strain fields), as well as on the elastic moduli of the inclusion and of the matrix [78]. The elastic dipole is related to the equivalent transformation strain through [29]

$$P_{ij} = \Omega C_{ijkl} e^{\mathrm{T}}_{kl}, \tag{A.1}$$

with

$$C_{ijkl} = \left(K - \frac{2}{3}\mu\right)\delta_{ij}\delta_{kl} + \mu\left(\delta_{ik}\delta_{jl} + \delta_{il}\delta_{jk}\right). \tag{A.2}$$

In SIPA-I models, the defect is considered as isotropic, so $e^{\mathrm{T}}_{kl} = \delta_{kl} e^{\mathrm{T}}/3$. We obtain

$$P_{ij} = \Omega K e^{\mathrm{T}} \delta_{ij} = P\delta_{ij}, \tag{A.3}$$

where P is the quantity used in Eqs. (6)-(10). It is customary to use the strain within the inclusion in the absence of external field, e^0_{ij}, related to e^{T}_{ij} by [78]

$$e^0_{ij} = \mathcal{S}_{ijkl} e^{\mathrm{T}}_{kl}, \tag{A.4}$$

where $\mathcal{S}_{ijkl}$ is the Eshelby tensor for a spherical inclusion:

$$\mathcal{S}_{ijkl} = \frac{5\nu - 1}{15(1-\nu)}\delta_{ij}\delta_{kl} + \frac{4 - 5\nu}{15(1-\nu)}\left(\delta_{ik}\delta_{jl} + \delta_{il}\delta_{jk}\right). \tag{A.5}$$

The strain within the inclusion can be written as $e^0_{kl} = \delta_{kl} e^0/3$, with

$$e^0 = \frac{1+\nu}{3(1-\nu)} e^{\mathrm{T}} = \frac{1+\nu}{3(1-\nu)} \frac{P}{\Omega K}. \tag{A.6}$$

We note that owing to Eqs. (17) and (A.3), e^{T} is the normalized relaxation volume in a finite medium $\Delta V^{\mathrm{r}}/\Omega$, whereas e^0 is the normalized relaxation volume in an infinite medium $\Delta V^{\infty}/\Omega$, the deformation being localized at the position of the point defect [79].

By comparing the expressions of the interaction energy given by Eshelby [78] and the one obtained from Eqs. (2) and (5), the following expressions are obtained:

$$\alpha^K = -K\Omega \frac{3(1-\nu)\Delta K}{3(1-\nu)K + (1+\nu)\Delta K} \tag{A.7}$$

$$\alpha^\mu = -\mu\Omega \frac{15(1-\nu)\Delta\mu}{15(1-\nu)\mu + 2(4-5\nu)\Delta\mu}, \tag{A.8}$$

with $\Delta K = K^* - K$ and $\Delta\mu = \mu^* - \mu$.

Appendix B. Set of deformation types to calculate polarizability tensors

The structure of the polarizability tensors of vacancies and SIAs in their stable and saddle configurations depend on their symmetries. They are given in Table B.2. To determine all coefficients, we consider several deformation types (Tab. B.3). Since both initial ([100]) and final ([010]) configurations must be relaxed under applied strain in order to calculate the saddle position, the results concerning the final configurations can also be exploited to obtain additional data about coefficients of the polarizability tensor.

Figures B.10 and B.11 show the variation of energy due to polarizability, called $E^{(2)}$ (see Tab. B.3) extracted from DFT simulations (solid lines) and calculated with the elastic model using polarizabilities deduced from residual stress (in dashed lines). The variation of residual stress due to polarizability, $-V\Delta\sigma_{ij} = \alpha_{ijkl}\varepsilon_{kl}$, is also shown. These two deformations (1 and 3, see Tab. B.3) correspond to dilatation/compression and ⟨100⟩ shear.

Table B.2
Structure of polarizability tensors of vacancies and SIAs in their stable and saddle configurations.

	Stable configuration	Saddle configuration
Vacancy	Cubic symmetry $\begin{pmatrix} \alpha_{11} & \alpha_{12} & \alpha_{12} & 0 & 0 & 0 \\ \alpha_{12} & \alpha_{11} & \alpha_{12} & 0 & 0 & 0 \\ \alpha_{12} & \alpha_{12} & \alpha_{11} & 0 & 0 & 0 \\ 0 & 0 & 0 & \alpha_{44} & 0 & 0 \\ 0 & 0 & 0 & 0 & \alpha_{44} & 0 \\ 0 & 0 & 0 & 0 & 0 & \alpha_{44} \end{pmatrix}$	Orthorhombic symmetry For [100] to [010] jump $\begin{pmatrix} \alpha_{11} & \alpha_{12} & \alpha_{13} & 0 & 0 & \alpha_{16} \\ \alpha_{12} & \alpha_{11} & \alpha_{13} & 0 & 0 & \alpha_{16} \\ \alpha_{13} & \alpha_{13} & \alpha_{33} & 0 & 0 & \alpha_{36} \\ 0 & 0 & 0 & \alpha_{44} & \alpha_{45} & 0 \\ 0 & 0 & 0 & \alpha_{45} & \alpha_{44} & 0 \\ \alpha_{16} & \alpha_{16} & \alpha_{36} & 0 & 0 & \alpha_{66} \end{pmatrix}$
SIA	Tetragonal symmetry For [100] configuration $\begin{pmatrix} \alpha_{11} & \alpha_{12} & \alpha_{12} & 0 & 0 & 0 \\ \alpha_{12} & \alpha_{22} & \alpha_{23} & 0 & 0 & 0 \\ \alpha_{12} & \alpha_{23} & \alpha_{22} & 0 & 0 & 0 \\ 0 & 0 & 0 & \alpha_{44} & 0 & 0 \\ 0 & 0 & 0 & 0 & \alpha_{55} & 0 \\ 0 & 0 & 0 & 0 & 0 & \alpha_{55} \end{pmatrix}$	Orthorhombic symmetry For [100] to [010] jump $\begin{pmatrix} \alpha_{11} & \alpha_{12} & \alpha_{13} & 0 & 0 & \alpha_{16} \\ \alpha_{12} & \alpha_{11} & \alpha_{13} & 0 & 0 & \alpha_{16} \\ \alpha_{13} & \alpha_{13} & \alpha_{33} & 0 & 0 & \alpha_{36} \\ 0 & 0 & 0 & \alpha_{44} & \alpha_{45} & 0 \\ 0 & 0 & 0 & \alpha_{45} & \alpha_{44} & 0 \\ \alpha_{16} & \alpha_{16} & \alpha_{36} & 0 & 0 & \alpha_{66} \end{pmatrix}$

Table B.3
Strain tensors and related variation in energies and dipole tensors due to polarizability. Tetragonal and orthorhombic symmetries refer to polarizability tensors given in Table B.2 ([100] orientation for the SIA and [100] to [010] jump respectively), unless specified.

strain matrix	cubic symmetry		tetragonal symmetry		orthorhombic symmetry	
	$-\frac{1}{2}\alpha_{ijkl}\varepsilon_{ij}\varepsilon_{kl}$	$-V\Delta\sigma_{ij}=\alpha_{ijkl}\varepsilon_{kl}$	$-\frac{1}{2}\alpha_{ijkl}\varepsilon_{ij}\varepsilon_{kl}$	$-V\Delta\sigma_{ij}=\alpha_{ijkl}\varepsilon_{kl}$	$-\frac{1}{2}\alpha_{ijkl}\varepsilon_{ij}\varepsilon_{kl}$	$-V\Delta\sigma_{ij}=\alpha_{ijkl}\varepsilon_{kl}$
$\boldsymbol{\varepsilon}_1=\begin{pmatrix}\varepsilon&0&0\\0&\varepsilon&0\\0&0&\varepsilon\end{pmatrix}$	$-\frac{3}{2}(\alpha_{11}+2\alpha_{12})\varepsilon^2$	$-V\Delta\sigma_{11}=(\alpha_{11}+2\alpha_{12})\varepsilon$	$-\frac{1}{2}(\alpha_{11}+2\alpha_{22}+4\alpha_{12}+2\alpha_{23})\varepsilon^2$		$-\frac{1}{2}(2\alpha_{11}+2\alpha_{12}+\alpha_{33}+4\alpha_{13})\varepsilon^2$	
$\boldsymbol{\varepsilon}_2=\begin{pmatrix}\varepsilon&0&0\\0&0&0\\0&0&0\end{pmatrix}$	$-\frac{1}{2}\alpha_{11}\varepsilon^2$				$-\frac{1}{2}\alpha_{11}\varepsilon^2$	
$\boldsymbol{\varepsilon}_3=\begin{pmatrix}0&0&0\\0&0&\varepsilon\\0&\varepsilon&0\end{pmatrix}$	$-2\alpha_{44}\varepsilon^2$	$-V\Delta\sigma_{23}=2\alpha_{44}\varepsilon$			$-2\alpha_{44}\varepsilon^2$	
$\boldsymbol{\varepsilon}_4=\begin{pmatrix}0&\varepsilon&0\\\varepsilon&0&0\\0&0&0\end{pmatrix}$	Equivalent to $\boldsymbol{\varepsilon}_3$		Equivalent to $\boldsymbol{\varepsilon}_3$ on final configuration		$-2\alpha_{66}\varepsilon^2$	

[a] On final configuration (SIA oriented along [010])

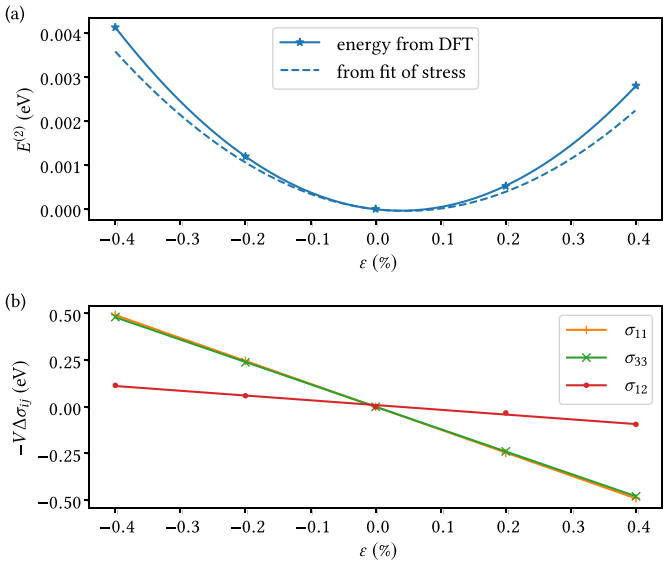

Fig. B.10. Deformation 1 (dilatation/compression): (a) Variation of energy due to polarizability, extracted from DFT simulations (symbols with fit in solid lines) and calculated with the elastic model using polarizabilities extracted from residual stress (dashed lines). (b) Variation of residual stress (*i. e.* change in dipole tensors) due to polarizability, which is fitted with a linear function to extract polarizabilities.

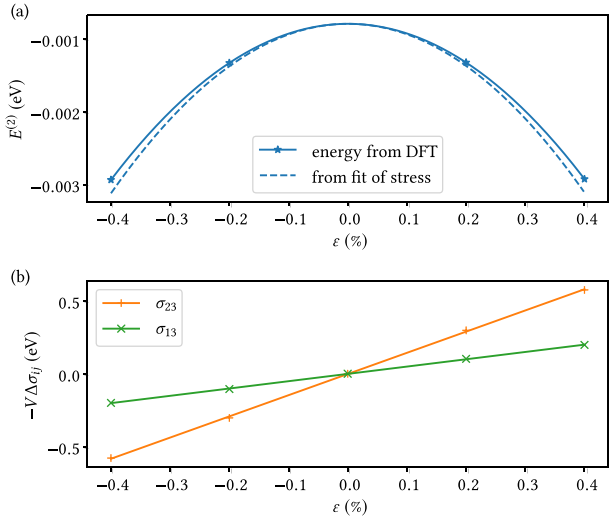

Fig. B.11. Deformation 3 ($\langle 100\rangle$ shear): (a) Variation of energy due to polarizability, extracted from DFT simulations (symbols with fit in solid lines) and calculated with the elastic model using polarizabilities extracted from residual stress (dashed lines). (b) Variation of residual stress (*i. e.* change in dipole tensors) due to polarizability, which is fitted with a linear function to extract polarizabilities.

Supplementary material

Supplementary material associated with this article can be found, in the online version, at doi:10.1016/j.actamat.2022.118431.

References

[1] J.R. Matthews, M.W. Finnis, Irradiation creep models – An overview, J. Nucl. Mater. 159 (1988) 257.
[2] F. Onimus, T. Jourdan, C. Xu, A.A. Campbell, M. Griffiths, 1.10 - Irradiation creep in materials, in: Comprehensive Nuclear Materials, Elsevier, 2020, p. 310.
[3] P.R. Okamoto, S.D. Harkness, Stress-biased loop nucleation in irradiated type 316 stainless steels, J. Nucl. Mater. 48 (1973) 204.
[4] F.A. Garner, W.G. Wolfer, H.R. Brager, A reassessment of the role of stress in development of radiation-induced microstructure, in: J.A. Sprague, D. Kramer (Eds.), Effects of radiation on structural materials, ASTM STP 683, 1979, p. 160.
[5] D. Faulkner, R.J. McElroy, Irradiation creep and growth in zirconium during proton bombardment, in: J.A. Sprague, D. Kramer (Eds.), Effects of Radiation on Structural Materials: ASTM STP 683, 1979, p. 329.
[6] F.A. Garner, D.S. Gelles, Irradiation creep mechanisms: an experimental perspective, J. Nucl. Mater. 159 (1988) 286.
[7] S. Jitsukawa, Y. Katano, K. Shiraishi, F.A. Garner, The Behavior of Irradiation-Produced Dislocation Loops under External Stress during Electron Irradiation, in: R.E. Stoller, A.S. Kumar, D.S. Gelles (Eds.), Effects of Radiation on Materials: 15th International Symposium, 1992, p. 1034.
[8] C. Xu, G.S. Was, Anisotropic dislocation loop distribution in alloy T91 during irradiation creep, J. Nucl. Mater. 454 (2014) 255.
[9] W.G. Wolfer, Correlation of radiation creep theory with experimental evidence, J. Nucl. Mater. 90 (1980) 175.
[10] W.G. Wolfer, L.K. Mansur, J.A. Sprague, Theory of swelling and irradiation creep, in: M.L. Bleiberg, J.W. Bennett (Eds.), Radiation Effects in Breeder Reactor Structural Materials, 1977, p. 479.
[11] L.K. Mansur, Irradiation creep by climb-enabled glide of dislocations resulting from preferred absorption of point defects, Philos. Mag. A 39 (1979) 497.
[12] C.H. Woo, E.J. Savino, Stress-induced preferred absorption due to saddle-point anisotropy: the case of an infinitesimal dislocation loop, J. Nucl. Mater. 116 (1983) 17.
[13] B.C. Skinner, C.H. Woo, Shape effect in the drift diffusion of point defects into straight dislocations, Phys. Rev. B 30 (1984) 3084.
[14] E.J. Savino, C.N. Tomé, Irradiation creep by stress-induced preferential attraction due to anisotropic diffusion (SIPA-AD), J. Nucl. Mater. 108 & 109 (1982) 405.
[15] C.N. Tomé, H.A. Cecatto, E.J. Savino, Point-defect diffusion in a strained crystal, Phys. Rev. B 25 (1982) 7428.
[16] C.H. Woo, Irradiation creep due to elastodiffusion, J. Nucl. Mater. 120 (1984) 55.
[17] V.A. Borodin, A.I. Ryazanov, The effect of diffusion anisotropy on dislocation bias and irradiation creep in cubic lattice materials, J. Nucl. Mater. 210 (1994) 258.
[18] H.R. Schober, Single and multiple interstitials in FCC metals, J. Phys. F: Metal Phys. 7 (1977) 1127.
[19] E.J. Savino, Point defect-dislocation interaction in a crystal under tension, Philos. Mag. 36 (1977) 323.
[20] P.H. Dederichs, K. Schroeder, Anisotropic diffusion in stress fields, Phys. Rev. B 17 (1978) 2524.
[21] P.T. Heald, M.V. Speight, Steady-state irradiation creep, Philos. Mag. 29 (1974) 1075.
[22] R. Bullough, J.R. Willis, The stress-induced point defect-dislocation interaction and its relevance to irradiation creep, Philos. Mag. 31 (1975) 855.
[23] P.T. Heald, M.V. Speight, Point defect behaviour in irradiated materials, Acta Metall. 23 (1975) 1389.

[24] W. Schilling, Self-interstitial atoms in metals, J. Nucl. Mater. 69 & 70 (1978) 465.
[25] C. Varvenne, E. Clouet, Elastic dipoles of point defects from atomistic simulations, Phys. Rev. B 96 (2017) 224103.
[26] D. Carpentier, T. Jourdan, Y. Le Bouar, M.-C. Marinica, Effect of saddle point anisotropy of point defects on their absorption by dislocations and cavities, Acta Mater. 136 (2017) 323.
[27] T. Jourdan, A. Vattré, A continuous model including elastodiffusion for sink strength calculation of interfaces, Comput. Mater. Sci. 153 (2018) 473.
[28] R. Siems, Mechanical interactions of point defects, Phys. Stat. Sol. 30 (1968) 645.
[29] E. Clouet, C. Varvenne, T. Jourdan, Elastic modeling of point-defects and their interactions, Comp. Mater. Sci. 147 (2018) 49.
[30] H.R. Schober, Polarizabilities of point defects in metals, J. Nucl. Mater. 126 (1984) 220.
[31] A.D. Brailsford, R. Bullough, The rate theory of swelling due to void growth in irradiated metals, J. Nucl. Mater. 44 (1972) 121.
[32] A.D. Brailsford, R. Bullough, M.R. Hayns, Point defect sink strengths and void-swelling, J. Nucl. Mater. 60 (1976) 246–256.
[33] F.A. Nichols, On the estimation of sink-absorption terms in reaction-rate-theory analysis of radiation damage, J. Nucl. Mater. 75 (1978) 32.
[34] C.H. Woo, The sink strength of a dislocation loop in the effective medium approximation, J. Nucl. Mater. 98 (1981) 279.
[35] T. Jourdan, Influence of dislocation and dislocation loop biases on microstructures simulated by rate equation cluster dynamics, J. Nucl. Mater. 467 (2015) 286.
[36] A.A. Kohnert, L. Capolungo, Sink strength and dislocation bias of three-dimensional microstructures, Phys. Rev. Mater. 3 (2019) 053608.
[37] W.G. Wolfer, M. Ashkin, Diffusion of vacancies and interstitials to edge dislocations, J. Appl. Phys. 47 (1976) 791.
[38] C.H. Woo, Effects of an anisotropic dislocation structure on irradiation creep due to stress induced preferred absorption of point defects, J. Nucl. Mater. 80 (1979) 132.
[39] P. Ehrhart, P. Jung, H. Schultz, H. Ullmaier, Landolt–Börnstein, Numerical Data and Functional Relationships in Science and Technology, Atomic Defects In Metals, Springer, 1991.
[40] I.-W. Chen, Anisotropic diffusion of point defects to edge dislocations, J. Nucl. Mater. 125 (1984) 52.
[41] G.F. Bouobda Moladje, L. Thuinet, C. Domain, C.S. Becquart, A. Legris, Phase–field calculations of sink strength in Al, Ni, and Fe: A detailed study of elastic effects, Comput. Mater. Sci. 183 (2020) 109905.
[42] V.A. Borodin, The effect of swelling on SIPA irradiation creep, J. Nucl. Mater. 225 (1995) 15.
[43] A. Vattré, T. Jourdan, H. Ding, M.-C. Marinica, M.J. Demkowicz, Non-random walk diffusion enhances the sink strength of semicoherent interfaces, Nat. Commun. 7 (2016) 10424.
[44] E. Clouet, A. Bakaev, V. Borodin, Z. Chang, C.C. Fu, M.C. Marinica, P. Olsson, M. Posselt, D. Terentyev, P. Vladimirov, E.E. Zhurkin, Screening of irradiation creep mechanisms using atomic-level simulation tools, Technical Report, MATISSE project, 2017.
[45] E. Clouet, S. Garruchet, H. Nguyen, M. Perez, C.S. Becquart, Dislocation interaction with C in α-Fe: A comparison between atomic simulations and elastic theory, Acta Mater. 56 (2008) 3450.
[46] G. Kresse, J. Hafner, *Ab initio* molecular dynamics for liquid metals, Phys. Rev. B 47 (1993) 558.
[47] G. Kresse, J. Hafner, *Ab initio* molecular-dynamics simulation of the liquid-metal–amorphous-semiconductor transition in germanium, Phys. Rev. B 49 (1994) 14251.
[48] G. Kresse, J. Furthmüller, Efficiency of ab-initio total energy calculations for metals and semiconductors using a plane-wave basis set, Comput. Mater. Sci. 6 (1996) 15.
[49] G. Kresse, J. Furthmüller, Efficient iterative schemes for *ab initio* total-energy calculations using a plane-wave basis set, Phys. Rev. B 54 (1996) 11169.
[50] P.E. Blöchl, Projector augmented-wave method, Phys. Rev. B 50 (1994) 17953.
[51] G. Kresse, D. Joubert, From ultrasoft pseudopotentials to the projector augmented-wave method, Phys. Rev. B 59 (1999) 1758.
[52] N. Chetty, M. Weinert, T.S. Rahman, J.W. Davenport, Vacancies and impurities in aluminum and magnesium, Phys. Rev. B 52 (9) (1995) 6313.
[53] G. Henkelman, B.P. Uberuaga, H. Jónsson, A climbing image nudged elastic band method for finding saddle points and minimum energy paths, J. Chem. Phys. 113 (2000) 9901.
[54] M.A. Caro, S. Schulz, E.P. O'Reilly, Comparison of stress and total energy methods for calculation of elastic properties of semiconductors, J. Phys.: Condens. Matter 25 (2013) 025803.
[55] G.J. Ackland, Theoretical study of the effect of point defects on the elastic constants of copper, J. Nucl. Mater. 152 (1988) 53.
[56] D. Connétable, P. Maugis, Effect of stress on vacancy formation and diffusion in fcc systems: Comparison between DFT calculations and elasticity theory, Acta Mater. 200 (2020) 869.
[57] V. Spirić, L.E. Rehn, K.-H. Robrock, W. Schilling, Anelastic relaxation due to single self-interstitial atoms in electron-irradiated Al, Phys. Rev. B 15 (1977) 672.
[58] K.-H. Robrock, W. Schilling, Diaelastic modulus change of aluminum after low temperature electron irradiation, J. Phys. F: Metal Phys. 6 (3) (1976) 303.
[59] P.H. Dederichs, C. Lehmann, A. Scholz, Change of elastic constants due to interstitials, Z. Physik B 20 (1975) 155.
[60] J. Holder, A.V. Granato, L.E. Rehn, Effects of self-interstitials and close pairs on the elastic constants of copper, Phys. Rev. B 10 (2) (1974) 363.
[61] L.E. Rehn, J. Holder, A.V. Granato, R.R. Coltman, F.W. Young Jr, Effects of thermal-neutron irradiation on the elastic constants of copper, Phys. Rev. B 10 (2) (1974) 349.
[62] M.P. Puls, C.H. Woo, Diaelastic polarizabilities due to vacancies and interstitials in metals, J. Nucl. Mater. 139 (1986) 48.
[63] H.-G. Haubold, Study of irradiation induced point defects by diffuse scattering, in: Proc. Int. Conf. Fundamental Aspects of Radiation Damage in Metals, 1975, p. 268.
[64] R.M. Emrick, P.B. McArdle, Effect of pressure on quenched-in electrical resistance in gold and aluminum, Phys. Rev. 188 (1969) 1156.
[65] P. Ehrhart, W. Schilling, Investigation of interstitials in electron-irradiated aluminum by diffuse-X-ray scattering experiments, Phys. Rev. B 8 (6) (1973) 2604.
[66] B.J. Buescher, R.M. Emrick, Pressure effect on defect migration in aluminum, Phys. Rev. B 1 (10) (1970) 3922.
[67] R.C. Folweiler, F.R. Brotzen, The effect of quenched-in vacancies on the elastic modulus of aluminum, Acta Metall. 7 (1959) 716.
[68] H.R. Brager, F.A. Garner, E.R. Gilbert, J.E. Flinn, W.G. Wolfer, Stress-affected microstructural development and the creep-swelling interrelationship, in: M.L. Bleiberg, J.W. Bennett (Eds.), Radiation Effects in Breeder Reactor Structural Materials, The Metallurgical Society of AIME, 1977, p. 727.
[69] W.P. Kuykendall, W. Cai, Conditional convergence in two-dimensional dislocation dynamics, Modelling Simul. Mater. Sci. Eng. 21 (2013) 055003.
[70] D.T. Gillespie, A general method for numerically simulating the stochastic time evolution of coupled chemical reactions, J. Comput. Phys. 22 (1976) 403.
[71] A.B. Bortz, M.H. Kalos, J.L. Lebowitz, A New Algorithm for Monte-Carlo Simulation of Ising Spin Systems, J. Comput. Phys. 17 (1975) 10.
[72] B. Zhang, C. Wheatley, P. Chen, X. Qian, M.J. Demkowicz, Shear strain alters the structure and migration of self-interstitial atoms in copper, Phys. Rev. Mater. 6 (2022) 053605.
[73] H. Flyvbjerg, H.G. Petersen, Error estimates on averages of correlated data, J. Chem. Phys. 91 (1989) 461.
[74] C.H. Woo, Intrinsic bias differential between vacancy loops and interstitial loops, J. Nucl. Mater. 107 (1982) 20.
[75] R. Bullough, M.R. Hayns, Irradiation-creep due to point defect absorption, J. Nucl. Mater. 57 (1975) 348.
[76] P.T. Heald, Radiation-induced creep and swelling, in: M.L. Bleiberg, J.W. Bennett (Eds.), Radiation Effects in Breeder Reactor Structural Materials, 1977, p. 781.
[77] C. Xu, G.S. Was, Proton irradiation creep of FM steel T91, J. Nucl. Mater. 459 (2015) 183.
[78] J.D. Eshelby, The determination of the elastic field of an ellipsoidal inclusion, and related problems, Proceedings of the Royal Society of London. Series A. Mathematical and Physical Sciences 241 (1957) 376.
[79] G. Leibfried, N. Breuer, Point Defects in Metals I, Springer Tracts in Modern Physics, Springer-Verlag, Berlin, 1978.